Chemical Physics Impact 7 (2023) 100362

Contents lists available at ScienceDirect

Chemical Physics Impact

journal homepage: www.sciencedirect.com/journal/chemical-physics-impact

Full Length Article

Fast microwave synthesis and white luminescent emission from $Pb_{1-2x}Ca_xSr_xMoO_4$ (x=0; 0.3; and 0.5) particles

C.R.D. Ferreira [a,*], A.A.G. Santiago [a], M.Siu Li [b], R.L. Tranquilin [c,d], F.V. Motta [a], M.R. D. Bomio [a,*]

[a] LSQM – Laboratory of Chemical Synthesis of Materials – Department of Materials Engineering, Federal University of Rio Grande do Norte, P.O. Box 1524, Natal, RN 59078-900, Brazil
[b] IFSC, USP, Av. Trabalhador São Carlense, 400, CEP, São Carlos, SP 13566-590, Brazil
[c] Department of Chemistry, CDMF-LIEC, Federal University of São Carlos, P.O Box 676, São Carlos, SP 135 65-905, Brazil
[d] Postgraduate Program in Biotechnology and Innovation in Health – University Anhanguera São Paulo (UNIAN), São Paulo, SP 05145-200, Brazil

ARTICLE INFO

Keywords:
Lead molybdate
Calcium
Strontium
Photoluminescence
White emission

ABSTRACT

Scheelite with ABO4 structure has been increasingly highlighted in the optoelectronic field. In this study, $PbMoO_4$, $Pb_{0.4}Ca_{0.3}Sr_{0.3}MoO_4$, and $Ca_{0.5}Sr_{0.5}MoO_4$ particles were fast synthesized via microwave-assisted hydrothermal method for 1, 2, 4, and 8 min. The particles were characterized by X-ray diffraction (XRD) and Rietveld refinement, ultraviolet-visible (UV–vis) absorption spectroscopy, photoluminescence (PL), and field emission scanning electron microscopy (FE-SEM). The diffractogram showed a scheelite-type tetragonal structure and a unit cell with space group $I4_1/a$, as well as the presence of defects with an increase in the synthesis time in $PbMoO_4$ and $Pb_{0.4}Ca_{0.3}Sr_{0.3}MoO_4$ samples. Rietveld refinement data possibilities the evaluation of distortions in the tetrahedral [MoO_4] clusters and FE-SEM images showed octahedral, spherical particles, and flower-like morphology due to the additions of calcium and strontium in the structure. The bandgap of the materials varied between 3.32 and 4.18 eV, which was affected by the increase in the presence of dopants in the materials. The photoluminescence presented by the PL emission spectral showed a typical emission peak in green with the PL signal intensity decreasing with the synthesis time increase for the PCSMO samples, and the longer the synthesis time, the higher the PL signal for CSMO samples. CCT coordinates have been calculated for all samples and its value exhibited that, overall emission is near white light. This parameter infers that $Pb_{0.4}Ca_{0.3}Sr_{0.3}MoO_4$ sample, synthesized in 1 min, may have potential application in commercial LEDs, due to near white emission and fast microwave synthesis.

1. Introduction

Photoluminescence (PL) has been used to investigate the structure and properties of active sites on the surface of metallic oxides due to its high sensitivity and non-destructive behavior. It is possible to study the electronic structure, optics, and photochemical properties of semiconductor materials through the PL spectrum, in which information such as surface oxygen vacancies and defects, as well as the efficiency of charge carrier capture, immigration, and transfer can be transmitted [1–3].

Nanomaterials encompass materials with high surface area in which at least one dimension is in the range of 1 to 100 nm and can be made of a single material or multiples. This class of materials can be produced according to desired properties through control of size, shape, proper functionalization, and synthesis conditions [4,5]. White LED light sources are possible thanks to the evolution of fluorescent nanomaterials which have adjustable optical properties [6].

Due to their remarkable energy conservation, white light-emitting diodes (white LEDs) are the object of great interest in studies [6]. Some of the advanced applications of white-light-emitting materials are in fluorescent sensors, illumination sources, the fields of display systems and information devices. The Commission Internationale de l'Eclairage (CIE) establishes that white-light-emitting nanoparticles should emit primary colors (blue, green and red) or two complementary ones in the visible spectrum with the required intensity [7].

Molybdates are a class of semiconductors that have a general formula

* Corresponding authors.
E-mail addresses: camyla.ferreira.083@ufrn.edu.br (C.R.D. Ferreira), mauricio.bomio@ufrn.br (M.R.D. Bomio).

https://doi.org/10.1016/j.chphi.2023.100362

Available online 2 November 2023

of $XMoO_4$ (X = Ca, Sr, and Pb) and can present a scheelite or wolframite structure. Molybdates are quite versatile and have studies showing their use as photoluminescent materials, light-emitting diodes (LED), supercapacitors, detectors, lasers, sensors, scintillators, optical fibers, energy storage, and photocatalysts [8–13]. Structurally, molybdates with a scheelite-type tetragonal structure present a cation connected to eight oxygen atoms forming an octahedron [XO_8] and a molybdenum atom connected to four oxygen atoms forming a tetrahedron [MoO_4], which makes these materials chemically stable and good hosts for dopants [12,14,15]. There is a relationship between the morphology of the material and its properties due to the morphological facets which are exposed crystalline planes on the material particle surface [16,17]. Depending on which facet is exposed and predominant in the morphology, it will modify the behavior of the material because each crystallographic plane presents a different bandgap [16,17].

Lead molybdate has a tetragonal crystal structure and is an optical transparent material which has been investigated for its intrinsic luminescence at room temperature [18]. It is the interactions between the Mo d states and O 2p orbitals that are the reason for the semiconductor properties of $PbMoO_4$ [19]. Calcium molybdate is also a highly transparent material, therefore it allows the light to pass through the material without interfering in its luminescence. $CaMoO_4$ with a scheelite structure has been used as an anode material for Li ion batteries, scintillators in medical devices, solid-state lasers and solar cells due to its great photoluminescence properties [20].

On the other hand, strontium molybdate presents spectra in the blue and green region, having excellent luminescent properties. The $[MoO_4]^{2-}$ tetrahedral unit in this material absorbs light energy in the UV region, contributing to photoluminescence properties [20]. Many studies have been carried out with a combination of different ions with the aim to produce a white-light-emitting $SrMoO_4$ [21].

The choice of synthesis method and its variables are crucial to achieve structural and morphological modifications and thereby obtain a material with optimized properties. Thus, several synthetic methods have been used to obtain molybdates such as the microemulsion method [22,23], precipitation method [24–26], combustion [12,13,27], solvothermal route [23,28], complex polymerization, sonochemistry method [29–32] and the hydrothermal method [16,33]. However, the microwave-assisted hydrothermal method has been used due to the ease of controlling the synthesis parameters, as well as the possibility to obtain diverse morphological shapes and nanostructures with a fast synthesis time [22,34–37].

The main reason for this work was to analyze the influence of various synthesis times and combinations in the morphology and photoluminescence properties of $PbMoO_4$ (PMO), $Pb_{0.4}Ca_{0.3}Sr_{0.3}MoO_4$ (PCSMO) and $Ca_{0.5}Sr_{0.5}MoO_4$ (CSMO) synthesized by the microwave-assisted hydrothermal method (MAH). In turn, the samples were characterized by X-ray diffraction (XRD) and Rietveld refinement, ultraviolet-visible (UV–vis) absorption spectroscopy, photoluminescence (PL) and field emission scanning electron microscopy (FE-SEM) to analyze the results.

2. Materials and methods

2.1. Synthesis

The $PbMoO_4$ (PMO), $Pb_{0.4}Ca_{0.3}Sr_{0.3}MoO_4$ (PCSMO) and $Ca_{0.5}Sr_{0.5}MoO_4$ (CSMO) particles were synthesized by the microwave-assisted hydrothermal method adapted of previous study [38]. A typical experimental procedure for PMO was performed as follows: 5×10^{-3} mol of molybdic acid (H_2MoO_4, Alfa Aesar, 85 %) were added and dissolved in 50 ml of distilled water, while a summation of 5×10^{-3} mol of lead nitrate ($Pb(NO_3)_2$, Sigma Aldrich, 99.5 %). For PCSMO and CSMO, calcium nitrate ($Ca(NO_3)_2$, Synth, 99 %) and strontium nitrate ($Sr(NO_3)_2$, Vetec, 99 %) were stoichiometrically (% mol) added and dissolved in 45 ml of distilled water. Next, the solution having the nitrates were added to the solution with the molybdic acid (H_2MoO_3, Alfa Aesar, 85 %) and the pH of 7 was reached using ammonium hydroxide (NH_4OH, Synth, 27 %). Then, the solution was transferred into a Teflon autoclave and was processed at 140 °C at times of 1, 2, 4, or 8 min. The resulting material was subsequently processed by the microwave-assisted hydrothermal method (2.45 GHz, maximum power of 800 W, 100 ml Teflon vessel, without stirring, with external temperature and power controller, with a constant pressure at 2 atm, and autoclaved was naturally at room temperature. The obtained solution was washed with distilled water and ethanol, and the precipitates were dried at 100 °C for 24 h.

2.2. Characterization

PMO, PCSMO, and CSMO particles were structurally characterized by XRD patterns, which were obtained with a Shimadzu XRD 7000 instrument with Cu-Kα radiation (λ = 1.5418 Å) in the 2θ range from 10° to 90° at a rate of 1° s^{-1}. The lattice parameters were calculated by adjustment of the experimental diffractogram with the use of the GSAS program [39]. The following parameters were refined: scaling factor and phase fraction; background (displaced Chebyshev polynomial function); peak shape (Thomson-Cox-Hasting pseudo-Voigt); change in the network constants; fractional atomic coordinates; and isotropic thermal parameters. Field emission scanning electron microscope (FE-SEM, Zeiss Supra 35-VP) was applied to analyze the particle morphology. UV–visible spectroscopy was recorded at 400–800 nm to show absorption and Tauc's equation was employed to compute the energy bandgap of the samples. Photoluminescence (PL) spectra were obtained by an Ash Monospec 27 monochromator (Thermal Jarrel, USA) and an R4446 photomultiplier (Hamamatsu Photonics, USA) was used to analyze the recombination process in the semiconductor particles, using 325 nm as the source of exciting wavelengths from a krypton ion laser.

3. Results and discussion

Fig. 1 shows the XRD patterns of $Pb_{1-2x}Ca_xSr_xMoO_4$ particles with x = 0, 0.3, and 0.5 synthesized by MAH at several different times. The PMO particles (Fig. 1a) have a tetragonal unit cell with space group $I4_1/a$ and characteristics diffraction peaks centered at an angle 27.5, 44.8, and 51.0 corresponding to (112), (204) and (116) planes, while CSMO particles (Fig. 1c) also have a tetragonal unit cell with space group $I4_1/a$ and diffraction peak characteristics centered at angles 28.1, 33.7, and 45.7 corresponding to (112), (004), and (204) planes, respectively. The samples were indexed by JCPDS Card no. 44–1486 and JCPDS Card no. 30–1287 which refers to the PMO and CaSrMO phases, respectively. As the synthesis times increased, there was a slight shift of the characteristic peaks to the left (Fig. 1a), which may indicate an increase in interplanar spacing and lattice parameters; furthermore, it is possible to confirm that the PMO powders are a well-crystallized and in pure phase for all times, suggesting an ordered structure over a long-range without the presence of a secondary phase. In Fig. 1b, the PCSMO samples synthesized from 1 to 4 min showed peaks between JCPDS Card no. 44–1486 and JCPDS Card no. 30–1287, indicating the formation of a phase composed of Pb^{2+}, Ca^{2+} and Sr^{2+} cations, meaning the formation of $Pb_{0.4}Ca_{0.3}Sr_{0.3}MoO_4$ solid solution, while the sample synthesized at 8 min presented formation of both phases of JCPDS Card no. 44–1486 and JCPDS Card no. 30–1287. Fig. 1c shows CSMO diffractograms characterized by the JCPDS Card no. 30–1287, in which no significant changes in the peaks were observed between the samples.

Rietveld refinement was used to investigate modifications in the structural arrangement induced by MAH processing of PMO, PCSMO, and CSMO (Figs. S1–S3). The refinement was done using the GSAS program, and the results are shown in Tables 1 and S1. As the difference between the curves observed (obs) and theoretically calculated (calc) was small, it can be concluded that the diffraction patterns are well-matched. The quality of the parameters can be measured from the

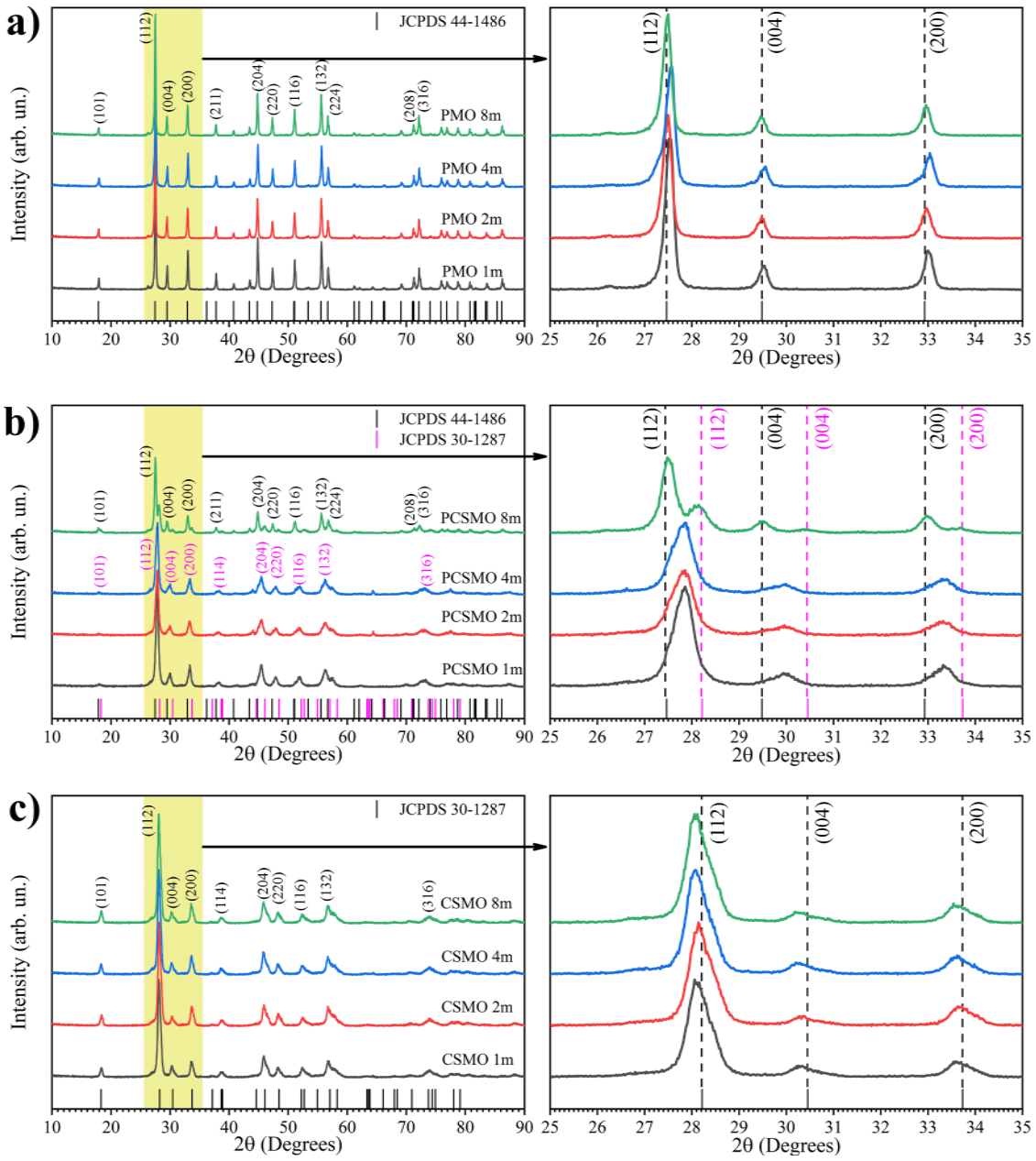

Fig. 1. XRD patterns of the PMO, PCSMO, and CSMO synthesized via microwave-assisted hydrothermal method for 1,2,4 and 8 min.

reliability parameters χ^2, R_{wp}, and R_p, with low values corresponding to good quality of the refinement.

Unit cell volume and structural lattice parameter values were similar to those found in the literature for scheelite tetragonal structure [30,34,40]. There were small variations in the e lattice parameter and unit cell volume values for the PMO and CSMO samples in all synthesis times in the same group, which indicates small lattice distortions, considering only the variation of synthesis time in the same group [41]. The PCSMO samples synthesized at 1, 2 and 4 min also did not show a large variation regardless of the synthesis time, however the PCSMO 8 m showed different lattice parameter and unit cell volume values as it presents two phases, not behaving as a solid solution anymore. Table 1 shows there was a decrease in the unit cell volume values, which is expected since Pb^{2+} has 1.29 Å as an ionic radius, larger than Ca^{2+} (1.12 Å) and Sr^{2+} (1.25 Å) [40,42,43]. An increase in the synthesis time led to a shift in the XRD towards smaller angles, indicating a raise in the interplanar distance. This augmentation in the interplanar distance could be associated with the higher volume of microwaves absorbed during the synthesis, which results in an anisotropic thermal expansion of these materials [44]. In this expansion, a more substantial enlargement is observed along the c-axis compared to the a-axis [44]. Additionally, as the synthesis time extends, there is an increased probability of nucleus formation and coalescence among particles, leading to a rise in the average particle size [45].

The crystallite size values decrease with increasing dopant concentration, which is attributed to the reduced numeric density of interatomic distances, leading to broadening of diffraction peaks [46,47]. The PMO samples showed crystallite size values varying from 38 nm to 48 nm, which is comparable to the values found by Song et al. [48] for $PbMoO_4$ synthetized by the microwave-assisted hydrothermal process. The PCSMO and CSMO samples showed similar crystallite size values varying from 8 nm to 19 nm and from 7 nm to 8 nm, respectively. The PCSMO samples synthesized at 1, 2 and 4 min have a similar behavior to solid state solutions, and according to Vergard's law, the unit cell dimensions can vary linearly with the solute component concentration [49,50]. Gaidamavičienė and Žalga [51] showed crystallite size values

Table 1
Rietveld refined parameters for PMO, PCSMO, and CSMO synthesized via microwave-assisted hydrothermal method at 1, 2, 4 and 8 min.

Compounds	PMO 1m	PMO 2m	PMO 4m	PMO 8m
Crystal system	Tetragonal	Tetragonal	Tetragonal	Tetragonal
Space group	$I4_1/a$	$I4_1/a$	$I4_1/a$	$I4_1/a$
a	5.432(2)	5.431(5)	5.432(4)	5.431(9)
c	12.11(8)	12.11(8)	12.12(1)	12.11(5)
V (Å^3)	357.6(0)	357.5(1)	357.7(09)	357.4(9)
χ^2	2.382	2.019	2.781	2.398
R_p	0.1485	0.1455	0.1748	0.1607
Rf^2	0.1505	0.1227	0.1153	0.1373
D_{hkl} (nm)	48	42	38	47
ε_{hkl} (x10^{-3})	0.39	0.45	0.51	0.40
Compounds	PCSMO 1m	PCSMO 2m	PCSMO 4m	PCSMO 8m
Crystal system	Tetragonal	Tetragonal	Tetragonal	Tetragonal
Space group	$I4_1/a$	$I4_1/a$	$I4_1/a$	$I4_1/a$
a	5.381(6)	5.383(05)	5.383(4)	5.430(6)*/ 5.327 (9)§
c	11.94(4)	11.94(9)	11.95(6)	12.11(1)*/ 11.76 (1)§
V (Å^3)	345.9(3)	346.2(4)	346.5(08)	357.1(8)*/ 333.8 (7)§
χ^2	1.403	1.645	1.640	1.303
R_p	0.1015	0.1186	0.1154	0.1036
Rf^2	0.0444	0.0676	0.0643	0.0811
D_{hkl} (nm)	9	8	8	19*/10§
ε_{hkl} (x10^{-3})	2.49	2.71	2.57	1.06*/2.05§
wt (%)				63.81*/36.19§
Compounds	CSMO 1m	CSMO 2m	CSMO 4m	CSMO 8m
Crystal system	Tetragonal	Tetragonal	Tetragonal	Tetragonal
Space group	$I4_1/a$	$I4_1/a$	$I4_1/a$	$I4_1/a$
a	5.330(9)	5.327(9)	5.329(8)	5.331(3)
c	11.78(8)	11.78(04)	11.78(6)	11.78(7)
V (Å^3)	335.0(3)	334.4(06)	334.8(1)	335.0(3)
χ^2	1.835	2.164	2.109	2.171
R_p	0.1241	0.1327	0.1293	0.1322
Rf^2	0.0501	0.0627	0.0500	0.0542
D_{hkl} (nm)	8	7	8	7
ε_{hkl} (x10^{-3})	2.81	3.19	2.90	3.07

Legend: *a* and *c* = lattice parameters (Å); *V* = unit cell volume; χ^2 = chi-squared; Rf^2 = structure factor squared; Rp = profile factor; *D* = crystallite size; ε = microstrain; wt (%) = weight fraction; * = $PbMoO_4$ phase; § = $Ca_{0.5}Sr_{0.5}MoO_4$ phase.

of 10.44 nm for $Ca_{0.5}Sr_{0.5}MoO_4$ synthesized by an aqueous sol-gel synthesis method at 400 °C.

Fig. 2 shows the [MoO_4] clusters and [Mo-O] bond length of PMO, PCSMO, and CSMO obtained from the atoms' position (Tables 1 and S1) by the Rietveld refinement data using the VESTA program [52]. The Mo-O bond length presented small variations from the PMO 1 min (Mo-*O* = 1.668 Å (4x)), PMO 2 min (Mo-*O* = 1.675 Å (4x)), PMO 4 min (Mo-*O* = 1.664 Å (4x)) and PMO 8 min (Mo-*O* = 1.675 Å (4x)). The bond length for the PCSMO samples also presented small variations between the PCSMO 1 min (Mo-*O* = 1.813 Å (4x)), PCSMO 2 min (Mo-*O* = 1.793 Å (4x)), and PCSMO 4 min (Mo-*O* = 1.822 Å (4x)) samples, while the PCSMO 8 min (Mo-*O* = 1.638 Å (4x), Mo-*O* = 1.860 Å (4x)) sample presented the smallest and biggest bond length for the PMO and CSMO phases, respectively. The CSMO samples also presented small variations of Mo-O bond length for the CSMO 1 min (Mo-*O* = 1.771 Å (4x)), CSMO 2 min (Mo-*O* = 1.776 Å (4x)) and CSMO 4 min (Mo-*O* = 1.770 Å (4x)) samples, while the CSMO 8 min (Mo-*O* = 1.738 Å (4x)) sample presented the smallest bond length value. According to the literature, molybdenum atom has tetrahedral coordination with Mo-O distances 1.77 Å and 1.75 Å in $PbMoO_4$ [53]; 1.810 Å and 1.79 Å in $CaMoO_4$ [54,55] and 1.79 Å in $SrMoO_4$ [55]. Variations in bond lengths can be associated with distortions in the [MoO_4] clusters. Thus, the changes in the MoO_4 clusters may be due to the different hydrothermal synthesis times for the PMO and CSMO samples, and solid solution formed by Pb^{2+}, Ca^{2+}, and Sr^{2+} cations in the PCSMO samples.

Fig. 3 shows the Raman spectra of PMO (a), PCSMO (b) and CSMO (c) from 150–1100 cm^{-1}. Considering the solution system as MXO_4 in which *M* = Pb, Ca e Sr and *X* = Mo, the nanoparticle precipitated as electron pair acceptors – M^{2+}cations reacted with the electron pair donors XO_4^{2-}. As a result of this interaction occurs the synthesis of MXO_4. According to Thongtem et al. [56], the Raman vibration for scheelite structure is expected to be:

$$\wp = 3Ag + 5Bg + 5Eg$$

The E mode is double degenerate, and the A and B are nondegenerate, as for the g, indicate the parity under inversion. The Raman vibrational external mode, lattice phonon, is for the motion of the cations (M^{2+}) to the anions (XO_4^{2-}). The internal mode is considered the stationary state of the mass center and corresponds to the vibration inside the tetrahedron (XO_4^{2-}). Tetrahedrons have T_d symmetry are composed of one free rotation mode ($\acute{\imath}_{f.r.}$(F1)), one translation mode (F2) and four internal modes ($\acute{\imath}_1$(A1), $\acute{\imath}_2$(E1), $\acute{\imath}_3$(F2) and $\acute{\imath}_4$(F2)), in free space. The point symmetry is reduced to S_4 when the tetrahedrons reside in the scheelite structure. The vibrations observed in the Raman spectra are summarized in Table 2.

The characteristic symmetric stretching pattern of the molybdates (υ_1 (Ag)) can be observed at 866, 871 and 880 cm^{-1}. As for a corresponding to vibrational modes of the antisymmetric stretches υ_3 (Bg) and υ_3 (Eg) can be identified, respectively, as 765 and 740 cm^{-1} (PMO and PCSMO 8 m), and 840 and 790 cm^{-1} (CSMO). The υ_4 (Eg) and υ_2 (Bg, Ag) peaks correspond to antisymmetric and symmetric stretching of the $[MO_4]^{2-}$. The $\acute{\imath}_{f.r.}(A_g)$ corresponding to the rotational and translational modes [38].

The FE-SEM images showed nano and micro-octahedral morphologies with well-defined edges in the PMO samples synthesized at 1, 2, 4, and 8 min processed by MAH, as can be seen in Fig. 4. According to the synthesis time, there were changes in the definition, size, and quantity of octahedrons. The crystals initially have an elevated level of agglomeration composed of nanometer-sized crystals. The growth of these crystals occurs in an orderly mode [57], which is similar to the oriented attachment mechanism for the PMO and PCSMO samples. In Fig. 4(a–d) it is possible to identify an octahedron-like morphology with well-defined faces of PMO particles. The PCSMO samples are shown in Fig. 4(e–h), in which these particles can be seen as expected in the presence of octahedral morphologies, as well as spherical and well-defined nanocrystals due to the characteristic of scheelite structure and presence of covalent Pb-O, Ca-O, and Sr-O bonds that are ionic and directional [57]. While synthesizing $SrMoO_4$ by the sonochemical method at 0.05 mol/L, Jiang et al. [31] observed the presence of spherical particles, with a similar morphology found in Fig. 4(e–h). PCSMO particles synthesized at 1, 2, and 4 min showed the presence of small nanocrystals; Ayni et al. [58] also described very small particles and an aggregate of particles as a result of lead molybdate synthesis via the co-precipitation method. Shen et al. [59] found sphere-like nanoparticles after synthesizing lead molybdate via the hydrothermal method at 140 °C, in which the addition of calcium and strontium atoms showed a loose nanoflake morphology for the PCSMO 8 min particles. The small size of PCSMO particles can be associated with the high-level impurity provoked by a solid solution of Pb^{2+}, Ca^{2+}, and Sr^{2+} cations in the same molybdate, where impurities perform a decrease in the potential barrier for the formation of nuclei and the growth velocities resulting in small particles [60]. The elemental mapping by EDX confirmed that the synthesis procedure based on hydrothermal microwave irradiation ensures a homogeneous distribution of elements on the particle surface (Fig. SI 4).

Ghaed-Amini et al. [25] observed the presence of hierarchical self-assembly $CaMoO_4$ nanostructures similar to the morphology found in all CSMO samples. Rahimi-Nasrabadi [61] described flower-like nanostructures formed by nanostructure morphology, as well as Hosseinpour-mashkani et al. [32], both while synthesizing strontium molybdate nanostructures. Similar morphology can be seen in Fig. 4 (i–l)

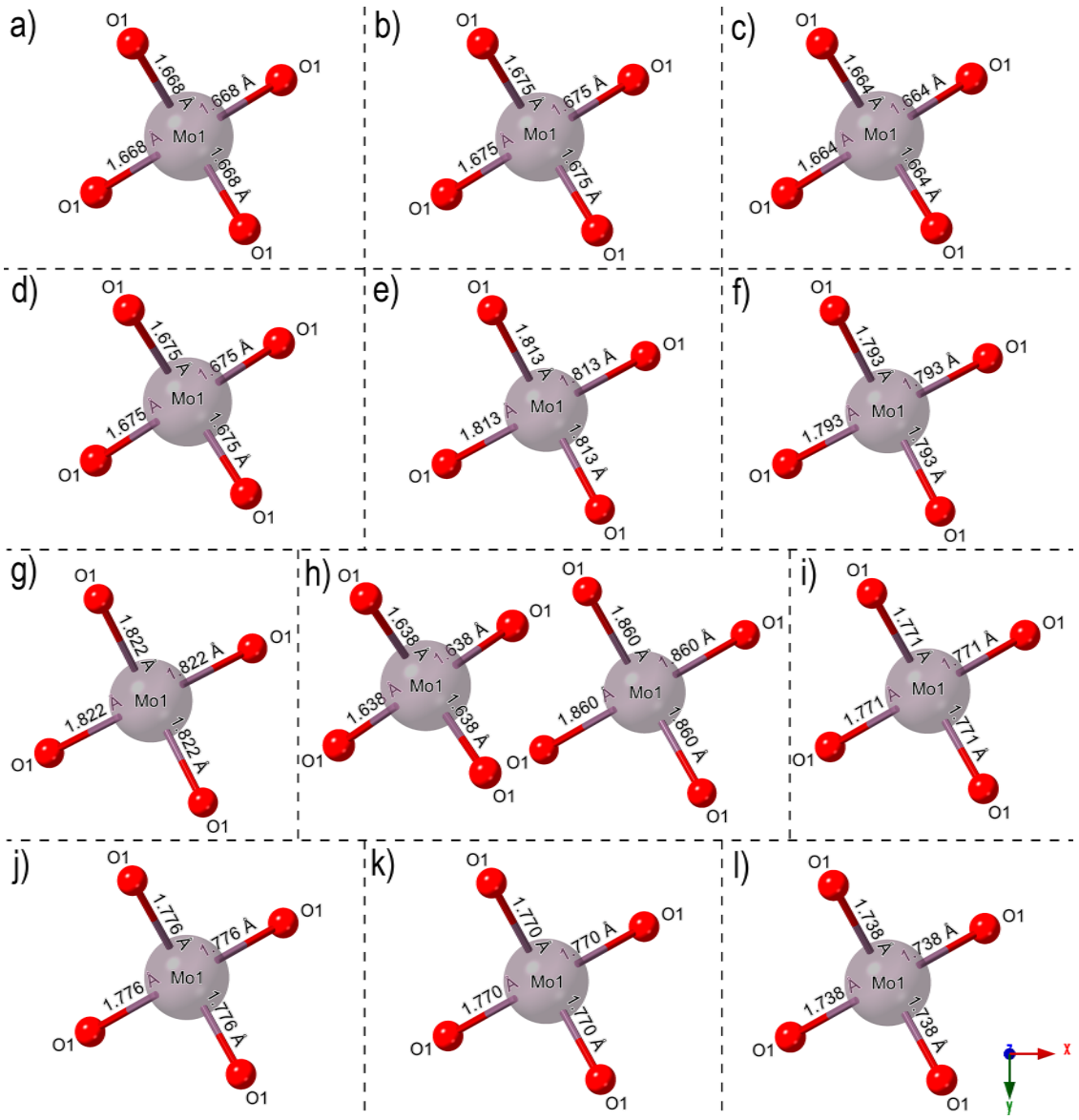

Fig. 2. Graphical representation of $[MoO_4]$ clusters and the [Mo-O] bond length of the $PbMoO_4$ and $Ca_{0.5}Sr_{0.5}MoO_4$ phases, namely (a) PMO 1 m, (b) PMO 2 m, (c) PMO 4 m, (d) PMO 8 m, (e) PCSMO 1 m, (f) PCSMO 2 m, (g) PCSMO 4 m, (h) PCSMO 8 m - $PbMoO_4$ phase is left and $Ca_{0.5}Sr_{0.5}MoO_4$ phase is right, (i) CSMO 1 m, (j) CSMO 2 m, (k) CSMO 4 m, and (l) CSMO 8 m.

in all CSMO particles.

Fig. 5 shows the images of the estimated band gap energy (E_{gap}) obtained by the diffuse reflectance spectroscopy technique in the visible ultraviolet for PMO, CSMO, and PCSMO at 1, 2, 4, and 8 min. The calculation was done using the Kubelka–Munk method described in Eq. (1):

$$F(R) = \frac{K}{S} = \frac{(1 - R)2}{2R} \quad (1)$$

In which: F(R) is the absorbance, K is the absorption coefficient, and S is the scattering coefficient. The Wood and Tauc [62] method (Eq. (2)) was used to estimate the bandgap values:

$$F(R)h\nu \propto (h\nu - E_{gap})^k \quad (2)$$

Considering the E_{gap} direct allowed in our work, $k = 1/2$ was adopted in Eq. (2). Fig. 5 illustrates the values of E_{gap} 3.32 eV for the PMO samples (Fig. 5a), 3.40–3.41 eV for PCSMO samples (Fig. 5b), and 4.12–4.18 eV for CSMO samples. PMO samples had values close to those found in the literature, such as 3.15 eV for PMO microcrystals synthesized with PVA, 3.03 and 3.23 eV for PMO synthesized using the sonochemistry method, 3.33 and 3.38 eV for PMO obtained via conventional hydrothermal synthesis, and 3.40 eV to 2D PbMoO4 nanosheet [33,41,63,64]. However, CSMO samples exhibited bandgap values falling within the range reported in the literature for $CaMoO_4$ and $SrMoO_4$ (3.75–4.16 eV) [20,65,66], with a value of 4.03 eV observed to CSMO synthetized via coprecipitation [67]. Polyhedron connectivity, the electronegativity of transitions metal ions, growth mechanism, distortions of the $[XO_4]^{2-}$, and deviation in O-X-O bonds are some facts which influence the energy bandgap and degree of structure order-disorder in the lattice. The emission phenomena for metal molybdates happen by the electronic charge transfer into $[XO_4]^{2-}$ units. The $[XO_4]^{2-}$ hybridization was originated by coupling between the O2p (σ) and O2p (π) ligand orbitals and Mo4d (t2) and Mo4d (e) orbitals for metal molybdates. A symmetry established from O2p (π) states presents t1 symmetry and is the top occupied state. The combination of a Mo4d (e) and O2p (π) with an *e* symmetry in turn is the lowest unoccupied state. The Mo4d for metal molybdate and O2p orbital hybridizations represent a covalent bond in the ions. The one-electron states below the

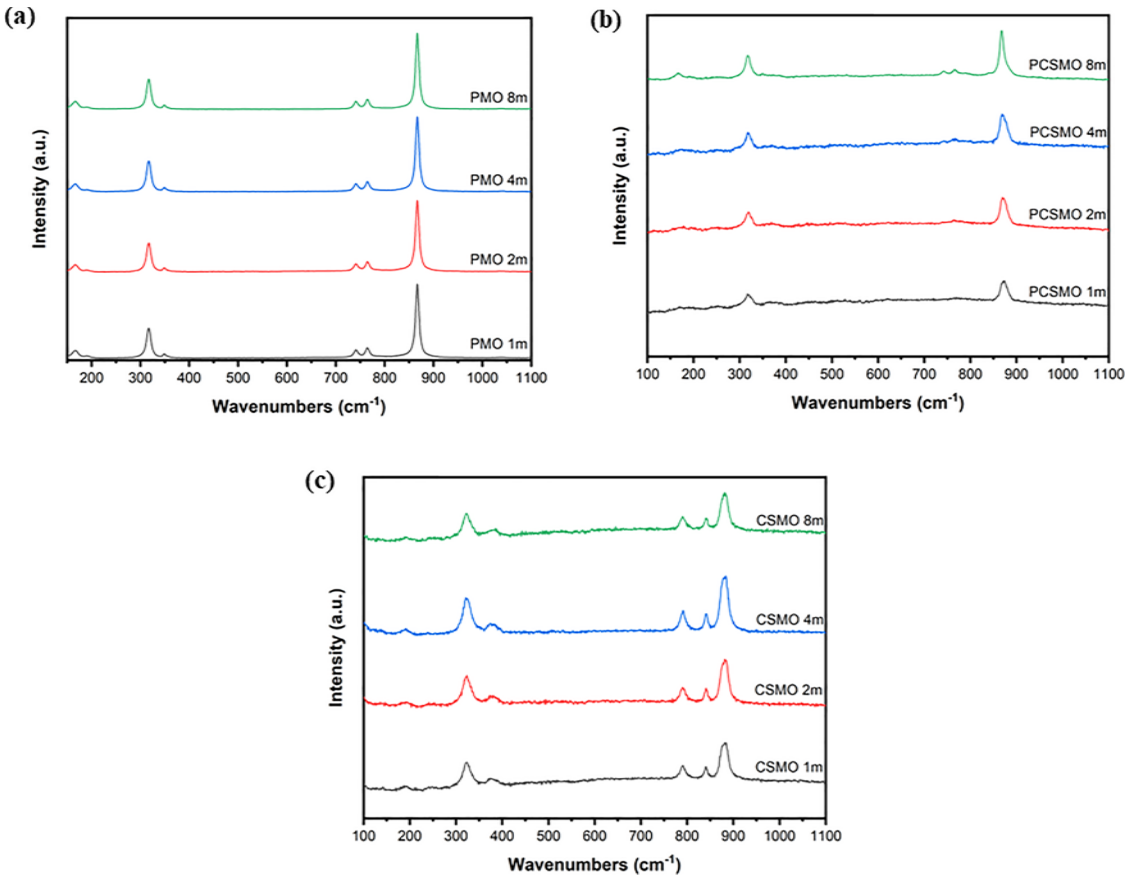

Fig. 3. Raman spectra of PMO (a), PCSMO (b) and CSMO (c).

Table 2
Raman wavenumbers of the products.

Lattice vibration	Wavenumber (cm^{-1})		
	PMO	PCSMO	CSMO
$í_1(A_g)$	866 (PMO 1 m)	—- (PCSMO 1 m)	880 (CSMO 1 m)
	866 (PMO 2 m)	—- (PCSMO 2 m)	880 (CSMO 2 m)
	866 (PMO 4 m)	—- (PCSMO 4 m)	880 (CSMO 4 m)
	866 (PMO 8 m)	871 (PCSMO 8 m)	880 (CSMO 8 m)
$í_3(B_g)$	765 (PMO 1 m)	—- (PCSMO 1 m)	840 (CSMO 1 m)
	765 (PMO 2 m)	—- (PCSMO 2 m)	840 (CSMO 2 m)
	765 (PMO 4 m)	—- (PCSMO 4 m)	840 (CSMO 4 m)
	765 (PMO 8 m)	765 (PCSMO 8 m)	840 (CSMO 8 m)
$í_3(E_g)$	740 (PMO 1 m)	—- (PCSMO 1 m)	790 (CSMO 1 m)
	740 (PMO 2 m)	—- (PCSMO 2 m)	790 (CSMO 2 m)
	740 (PMO 4 m)	—- (PCSMO 4 m)	790 (CSMO 4 m)
	740 (PMO 8 m)	740 (PCSMO 8 m)	790 (CSMO 8 m)
$í_4(B_g)$	349 (PMO 1 m)	—- (PCSMO 1 m)	379 (CSMO 1 m)
	349 (PMO 2 m)	—- (PCSMO 2 m)	379 (CSMO 2 m)
	349 (PMO 4 m)	—- (PCSMO 4 m)	379 (CSMO 4 m)
	349 (PMO 8 m)	—- (PCSMO 8 m)	379 (CSMO 8 m)
$í_2(A_g)$	316 (PMO 1 m)	317 (PCSMO 1 m)	322 (CSMO 1 m)
	316 (PMO 2 m)	317 (PCSMO 2 m)	322 (CSMO 2 m)
	316 (PMO 4 m)	317 (PCSMO 4 m)	322 (CSMO 4 m)
	316 (PMO 8 m)	317 (PCSMO 8 m)	322 (CSMO 8 m)
$í_{f.r.}(A_g)$	167 (PMO 1 m)	—- (PCSMO 1 m)	189 (CSMO 1 m)
	167 (PMO 2 m)	—- (PCSMO 2 m)	189 (CSMO 2 m)
	167 (PMO 4 m)	—- (PCSMO 4 m)	189 (CSMO 4 m)
	167 (PMO 8 m)	167 (PCSMO 8 m)	189 (CSMO 8 m)

bandgap are filled to show a many-electron $^1A_1$ state for the ground-state system. Many-electron $^1T_1$, $^3T_1$, $^1T_2$ and $^3T_2$ states are the result of one hole in the t1 (primarily O2p (π)) state and one-electron in the *e* (primarily Mo4d for metal molybdates) state for the lowest excited state. The only admitted transition is $^1T_2 \rightarrow {}^1A_1$ [56].

Bi et al. [10] synthesized $PbMoO_4$ and $SrMoO_4$ by the solvothermal method, and reported that the $PbMoO_4$ material should have a narrow bandgap, while the Pb 2 s and O 2p states introduce some divided states. The largest dispersion of $PbMoO_4$ is a result of the covalent interaction of Pb-O atoms. However, PCSMO samples showed an intermediate bandgap between PMO and CSMO samples and could have been influenced by the presence of Pb^{2+}, $Ca^{2+,}$ and Sr^{2+} cations in the same structure. Doping is a possible way to have a bandgap reduction in this type of metal molybdate [64]. So, the absorption of CSMO samples under UV-light is higher than those for PMO and PCSMO, which is important, as higher absorption must promote the electron-hole pairs to perform the redox reactions and a high PL intensity is related to a high recombination of the photogenerated charges. In comparison, as the CSMO samples can absorb more photons than PMO and PCSMO samples, they can present better photocatalytic activity [40]

Fig. 6 shows the PL spectra of the PMO, CSMO, and PCSMO particles prepared by the microwave-assisted process at different synthesis times. The PL spectra depend on the crystallinity and morphology of the crystals [23,41]. The emission spectra of the metal molybdates are mostly affected by charged transitions in $[XO_4]^{2-}$ complexes, distortions of the $[XO_4]^{2-}$ groups caused by particles sizes, crystalline degree, different angles of O-X-O, surface defects and morphology [22,56,68]. The Mo atom in the molybdate structure is four-fold coordinated with surrounding oxygen atoms and the MoO_4 tetrahedral units are observed [10]. The increase in ionic radius may be related to the PL intensity, since changes in the parable are related to the ionic radius of the cation. The deviation in the parabola is greater the greater the ionic radius of the cation, thus the greater the chance of non-radioactive transition from the exit state, the lower the radioactive transition intensity is [55].

As claimed by Blasse and Grabmaier [69], PL emission emerges from a return of radiative emission to the fundamental state, which is in

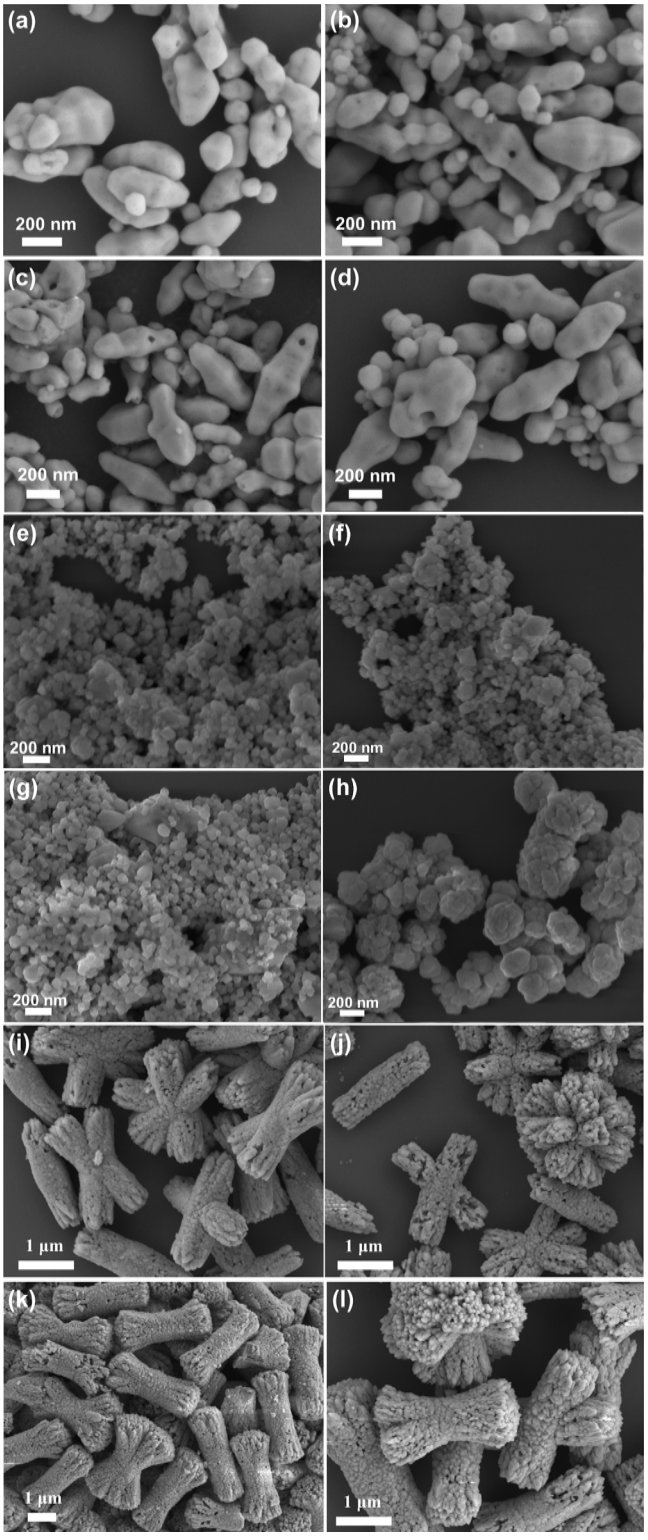

Fig. 4. FE-SEM images for PMO during a) 1, b) 2, c) 4, and d) 8 min; PCSMO during e) 1, f) 2, g) 4, and h) 8 min; CSMO during i) 1, j) 2, k) 4, and l) 8 min.

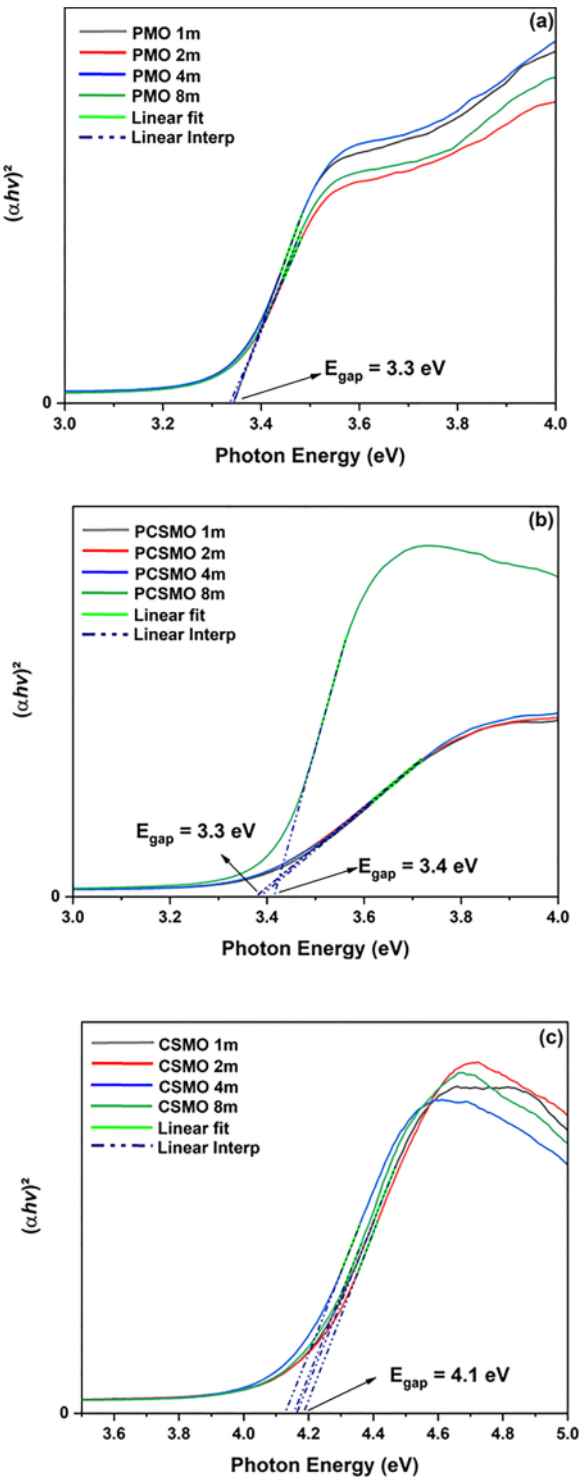

Fig. 5. Illustration of modified Kubelka-Munk function for determination of direct Egap of the a) PMO, b) PCSMO, and c) CSMO synthesized via microwave-assisted hydrothermal method during 1,2,4 and 8 min.

agreement with the non-radiative decay to the ground state. Vibration occurs in the non-radiative process and heating of the crystalline material lattice by the energy of the excited state. The structural disorder of $[MoO_4]^{2-}$, existence of oxygen vacancies, and generation of band gap intermediary energy levels are favored by the high concentration of defects, which increases the chance of non-radioactive transitions, and in turn intensifies the decrease of the PL emission. The luminescence of the material also can be a result of the transition in MoO_4 from the lowest $^3T_1$ and $^3T_2$ states to the $^1A_1$ state. The luminescence shows emission bands between the $^3T_1$ and $^3T_2$ triplet states [38].

According to the spectra obtained, all samples have a typical emission peak in green at 530, 535, and 540 nm, respectively. Green emissions are assigned to a more ordered structure and shallow defects in the band gap [12]. Deep and shallow defects can be related to the bandgap energy of the sample surface, where surfaces with higher bandgap

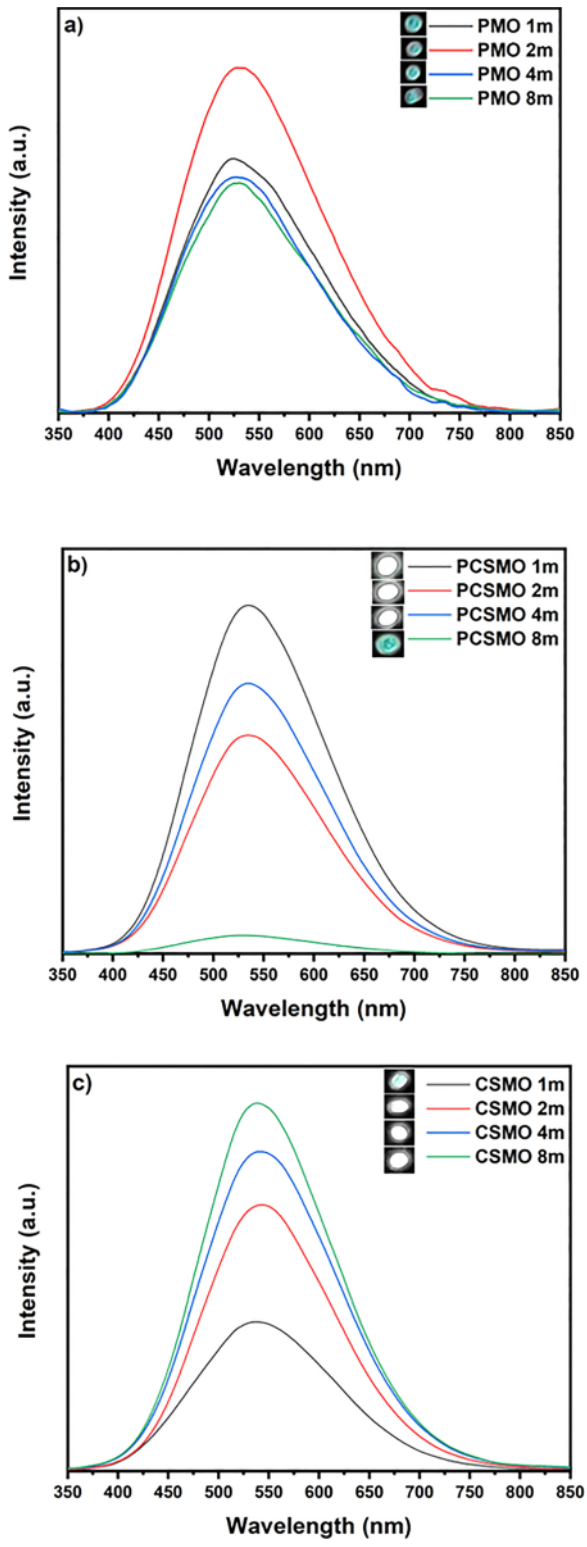

Fig. 6. PL emission spectrum of the a) PMO, b) PCSMO, and c) CSMO particles.

values are related to shallow defects and surfaces with lower bandgap values are related to deep defects. Thus, the deep defects of the PMO samples may be related to on the (001) surface due to its lower band gap energy (Egap = 3.56 eV), while shallow defects may be associated with from (011) surface and from (112) surface due to higher band gap energy values (Egap = 3.62 eV and Egap = 3.60 eV, respectively) [36]. Nevertheless, the deep defects of the CSMO samples may be related to from the surface (112) due to its smaller gap energy (Egap = 4.44 eV), while shallow defects may be associated with from the surface (011) and from the surface (001) due to higher values of band gap energy (Egap = 4.69 eV and Egap = 4.66 eV, respectively) [36]. Lastly, the deep defects of PCSMO samples may be related to of the surface (001) due to its lower band gap energy (Egap = 3.56 eV), while shallow defects may be associated with from the surface (011) and from the surface (112) due to higher values of band gap energy (Egap = 3.80 eV and Egap = 3.77 eV, respectively) [36]. The PL signal in the PCSMO samples decreased with increasing synthesis time, while longer synthesis times increased the PL signal for the CSMO sample. The Pb^{2+}, Ca^{2+}, and Sr^{2+} cations in the MoO_4^{2-} complex act as lattice modifying agents [34].

The illustration in Fig. 7 shows the PL emission according to the transitions in the $[MoO_4]^{2-}$. The $^1A_1$ state corresponds to the ground-state system, and $^1T_1$, $^3T_1$, $^1T_2$ and $^3T_2$ states symmetries correspond to the lowest excited states. The material intrinsic morphology is a result of the lowest excited states $^3T_1$ and $^3T_2$ to the ground $^1A_1$ state, while the transition $^1A_1 \leftrightarrow {}^1T_2$ is a dipole allowed transition [38]

Fig. 8 illustrates the CIE positions for PMO, PCSMO and CSMO particles. Table 3 shows the CIE coordination values, coordination color temperature (CCT) values and emission color for the samples. The PMO 1 min presented pure white, between daylight and sunlight color emission. The PMO 2 min, PMO 8 min, and PCSMO 8 min samples presented between daylight and sunlight color emission. The PMO 4 min presented bright mid-summer sunlight color emission. The PCSMO 1 min, PCSMO 2 min, PCSMO 4 min and CSMO 1 min samples presented bright daylight color emission. The CSMO 2 min and CSMO 8 min samples presented daylight color emission, and the CSMO 4 min sample presented daylight color emission. Therefore, several samples presented CCT values close to pure white, meaning CCT close to 5500 K, which indicates a possible application in commercial LEDs.

4. Conclusions

In summary, this study showed the efficiency of the microwave-assisted hydrothermal synthesis method for obtaining PMO, PCSMO, and CSMO particles. XRD results showed a tetragonal scheelite structure with the presence of a secondary phase only in the PCSMO 8 m sample. The influence of the synthesis times was seen through a small reduction in the XRD intensity of the PMO and PCSMO characteristic peaks as the synthesis times increased, which can indicate a decrease in the order of the structure. The FE-SEM images show the presence of octahedral morphologies, as well as spherical particles and flower-like morphology due to the calcium and strontium additions in the structure. The PMO's E_{gap} (3.32 eV) showed values close to those found in literature, while the CSMO's E_{gap} (4.12–4.18 eV) exhibited bandgap values falling within the range reported in the literature for $CaMoO_4$ and $SrMoO_4$. The PL emission results showed a typical emission peak in green with the PL signal intensity decreasing with the synthesis time increase for the PCSMO samples, while the longer the synthesis time for the CSMO samples, the higher the PL signal. A possible application in commercial LEDs was

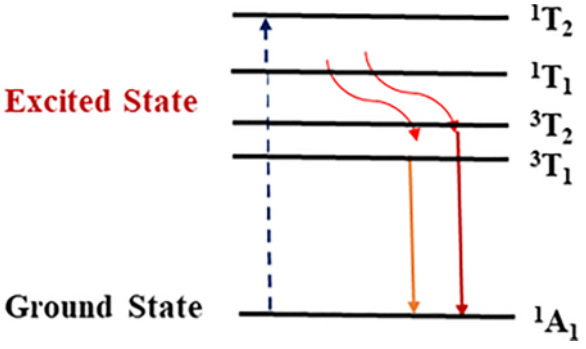

Fig. 7. Illustration of a transition state diagram.

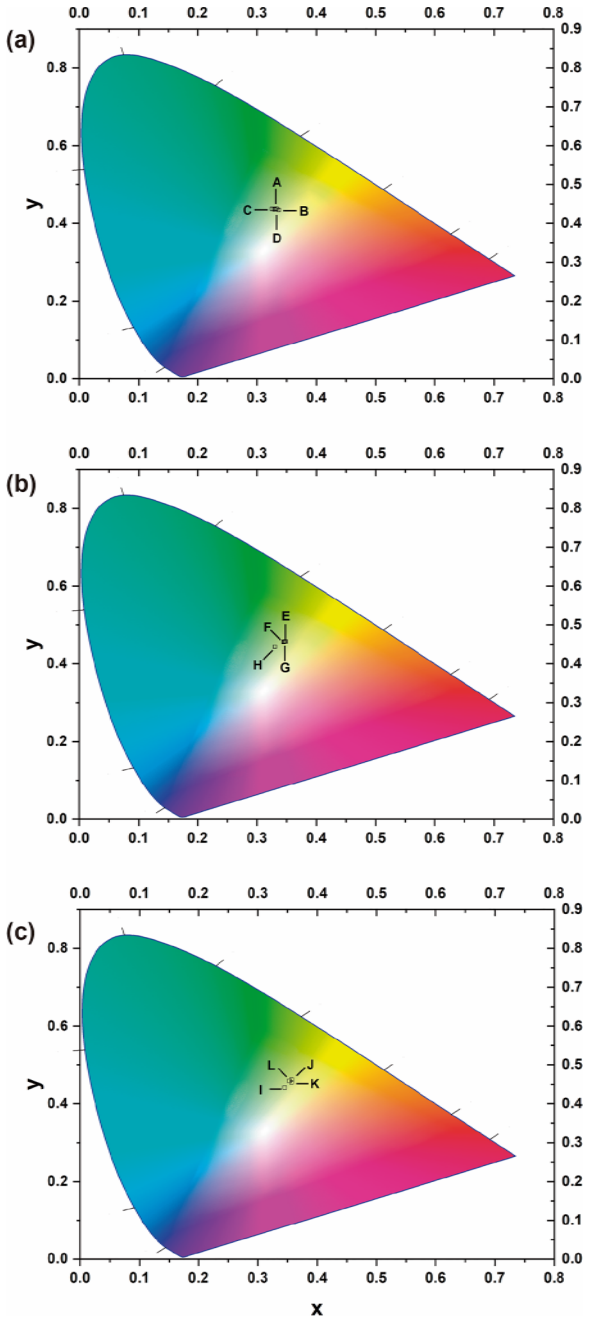

Fig. 8. CIE diagram for PMO, PCSMO, and CSMO particles.

observed in the PCSMO 1 m sample, in which the CCT values were close to pure white and presented a fast microwave synthesis.

CRediT authorship contribution statement

C.R.D. Ferreira: Data curation, Writing – original draft, Formal analysis, Investigation. **A.A.G. Santiago:** Writing – review & editing. **M. Siu Li:** Investigation, Resources. **R.L. Tranquilin:** Investigation, Resources. **F.V. Motta:** Methodology, Supervision, Resources. **M.R.D. Bomio:** Conceptualization, Methodology, Supervision, Writing – review & editing, Resources.

Declaration of Competing Interest

The authors declare that they have no known competing financial interests or personal relationships that could have appeared to influence the work reported in this paper.

Table 3
CIE and correlated temperature color (CCT) for PMO, PCSMO, and CSMO synthesized via microwave-assisted hydrothermal method during 1, 2, 4 and 8 min.

Code	Samples	CIE (x',y')	CCT (K)	Color
A	PMO 1m	(0.332, 0.437)	5521	Pure white, between daylight and sunlight
B	PMO 2m	(0.336, 0.434)	5401	Between daylight and sunlight
C	PMO 4m	(0.325, 0.436)	5711	Bright mid-summer sunlight
D	PMO 8m	(0.329, 0.435)	5600	Between daylight and sunlight
E	PCSMO 1m	(0.348, 0.457)	5149	Bright daylight
F	PCSMO 2m	(0.345, 0.456)	5218	Bright daylight
G	PCSMO 4m	(0.346, 0.457)	5188	Bright daylight
H	PCSMO 8m	(0.330, 0.444)	5585	Between daylight and sunlight
I	CSMO 1m	(0.345, 0.441)	5188	Bright daylight
J	CSMO 2m	(0.357, 0.462)	4953	Daylight
K	CSMO 4m	(0.357, 0.455)	4942	Daylight
L	CSMO 8m	(0.353, 0.458)	5028	Daylight

Data availability

Data will be made available on request.

Acknowledgments

The authors thank the following Brazilian research financing institutions for financial support: National Council for Scientific and Technological Development - CNPq (Process 305279/2020–3), Graduate Program in Materials Science and Engineering (PPGCEM-UFRN) and Coordination for the Improvement of Higher Education Personnel - Brazil (CAPES) - Finance Code 001.

Supplementary materials

Supplementary material associated with this article can be found, in the online version, at doi:10.1016/j.chphi.2023.100362.

References

[1] C. Colvard, PL: Photoluminescence, Encyclopedia of Materials Characterization, Elsevier, 1992, pp. 373–384.
[2] R. Karthick, P. Sakthivel, C. Selvaraju, M.S. Paulraj, Tuning of photoluminescence and antibacterial properties of ZnO nanoparticles through Sr doping for biomedical applications, J. Nanomater. 2021 (2021) 1–7.
[3] P. Binu, S. Muthukumaran, R.C. Ganesh, P. Sakthivel, Enhanced orange emission of $Zn_{0.98-X}Mn_{0.02}Co_xS$ ($x = 0 \leq 0.02$) quantum dots, J. Phys. Chem. Solids 160 (2022), 110370.
[4] N. Baig, I. Kammakakam, W. Falath, Nanomaterials: a review of synthesis methods, properties, recent progress, and challenges, Mater. Adv. 2 (2021) 1821–1871.
[5] V. Harish, D. Tewari, M. Gaur, A.B. Yadav, S. Swaroop, M. Bechelany, A. Barhoum, Review on nanoparticles and nanostructured materials: bioimaging, biosensing, drug delivery, tissue engineering, antimicrobial, and agro-food applications, Nanomater 12 (2022) 457.
[6] Q. Zhang, C.F. Wang, L.T. Ling, S. Chen, Fluorescent nanomaterial-derived white light-emitting diodes: what's going on, J. Mater. Chem. C 2 (2014) 4358–4373.
[7] Y. Hu, X. Liang, D. Wu, B. Yu, Y. Wang, Y. Mi, Z. Cao, Z. Zhao, Towards white-light emission of fluorescent polymeric nanoparticles with a single luminogen possessing AIE and TICT properties, J. Mater. Chem. C 8 (2020) 734–741.

[8] A. Phuruangrat, S. Thongtem, T. Thongtem, Synthesis and characterization of Gd-doped $PbMoO_4$ nanoparticles used for UV-light-driven photocatalysis, J. Rare Earths (2020).

[9] A. Mobeen, C.M. Magdalane, S.J. Shahina, D. Lakshmi, R. Sundaram, G. Ramalingam, A. Raja, J. Madhavan, D. Letsholathebe, A. Bashir, Investigation on antibacterial and photocatalytic degradation of Rhodamine-B dye under visible light irradiation by titanium molybdate nanoparticles prepared via microwave method, Surf. Interfaces 17 (2019), 100381.

[10] J. Bi, L. Wu, Y. Zhang, Z. Li, J. Li, X. Fu, Solvothermal preparation, electronic structure and photocatalytic properties of $PbMoO_4$ and $SrMoO_4$, Appl. Catal. B Environ. 91 (2009) 135–143.

[11] A. Santiago, Y. Fernandes, R. Tranquilin, E. Longo, C. Paskocimas, F. Motta, M. Bomio, Influence of $Zn_{1-x}Ca_xWO_4$ heterostructures synthesized by spray pyrolysis on photoluminescence property, Ceram. Int. 45 (2019) 23256–23264.

[12] S. Vidya, S. Solomon, J. Thomas, Synthesis, sintering and optical properties of $CaMoO_4$: a promising scheelite LTCC and photoluminescent material, Phys. Status Solidi 209 (2012) 1067–1074.

[13] M. Minakshi, D.R. Mitchell, C. Baur, J. Chable, A.J. Barlow, M. Fichtner, A. Banerjee, S. Chakraborty, R. Ahuja, Phase evolution in calcium molybdate nanoparticles as a function of synthesis temperature and its electrochemical effect on energy storage, Nanoscale Adv. 1 (2019) 565–580.

[14] W. Du, L. Liu, K. Zhou, X. Ma, Y. Hao, X. Qian, Black lead molybdate nanoparticles: facile synthesis and photocatalytic properties responding to visible light, Appl. Surf. Sci. 328 (2015) 428–435.

[15] L.X. Lovisa, A.A.G. Santiago, M.B. Farias, B.S. Barros, E. Longo, M.S. Li, C. A. Paskocimas, M.R.D. Bomio, F.V. Motta, White light emission from single-phase Y_2MoO_6: xPr^{3+} (x = 1, 2, 3 and 4 mol%) phosphor, J. Alloy. Compd. 769 (2018) 420–429.

[16] K. Dai, Y. Yao, H. Liu, I. Mohamed, H. Chen, Q. Huang, Enhancing the photocatalytic activity of lead molybdate by modifying with fullerene, J. Mol. Catal. A Chem. 374 (2013) 111–117.

[17] M. Hashim, C. Hu, X. Wang, X. Li, D. Guo, Synthesis and photocatalytic property of lead molybdate dendrites with exposed (0 0 1) facet, Appl. Surf. Sci. 258 (2012) 5858–5862.

[18] D.A. Spassky, S.N. Ivanov, V.N. Kolobanov, V.V. Mikhailin, V.N. Zemskov, B. I. Zadneprovski, L.I. Potkin, Optical and luminescent properties of the lead and barium molybdates, Radiat. Meas. 38 (2004) 607–610.

[19] L. Wang, H. Tang, Y. Tian, Carbon-shell-decorated p-semiconductor $PbMoO_4$ nanocrystals for efficient and stable photocathode of photoelectrochemical water reduction, J. Power Sources 319 (2016) 210–218.

[20] R. Karthik, N. Karikalan, S.M. Chen, J.V. Kumar, C. Karuppiah, V. Muthuraj, Assessment of divergent functional properties of seed-like strontium molybdate for the photocatalysis and electrocatalysis of the postharvest scald inhibitor diphenylamine, J. Catal. 352 (2017) 606–616.

[21] D. Dos Santos, L. Lovisa, A. Santiago, M.S. Li, E. Longo, M. Bomio, F. Motta, Growth mechanism and vibrational and optical properties of $SrMoO_4$:tb^{3+}, Sm^{3+} particles: green-orange tunable color, J. Mater. Sci. 55 (2020) 8610–8629.

[22] A. Phuruangrat, T. Thongtem, S. Thongtem, Synthesis of lead molybdate and lead tungstate via microwave irradiation method, J. Cryst. Growth 311 (2009) 4076–4081.

[23] G.J. Xing, R. Liu, C. Zhao, Y.L. Li, Y. Wang, G.M. Wu, Photoluminescence and photocatalytic properties of uniform $PbMoO_4$ polyhedral crystals synthesized by microemulsion-based solvothermal method, Ceram. Int. 37 (2011) 2951–2956.

[24] V. Anandakumar, M.A. Khadar, Microhardness studies of nanocrystalline lead molybdate, Mater. Sci. Eng. A 519 (2009) 141–146.

[25] M. Ghaed-Amini, M. Bazarganipour, M. Salavati-Niasari, Calcium molybdate octahedral nanostructures, hierarchical self-assemblies controllable synthesis by coprecipitation method: characterization and optical properties, J. Ind. Eng. Chem. 21 (2015) 1089–1097.

[26] M. Ghaed-Amini, M. Bazarganipour, M. Salavati-Niasari, Large scale synthesis of novel flower-like strontium molybdate nanostructures via co-precipitation method, J. Mater. Sci. Mater. Electron. 26 (2015) 7452–7459.

[27] T. Groń, M. Maciejkowicz, E. Tomaszewicz, M. Guzik, M. Oboz, B. Sawicki, S. Pawlus, A. Nowok, Z. Kukuła, Combustion synthesis, structural, magnetic and dielectric properties of Gd^{3+}-doped lead molybdato-tungstates, J. Adv. Ceram. (2020) 1–14.

[28] D. Hernández-Uresti, A. Martínez-de la Cruz, L. Torres-Martínez, Photocatalytic degradation of organic compounds by $PbMoO_4$ synthesized by a microwave-assisted solvothermal method, Ceram. Int. 42 (2016) 3096–3103.

[29] A. Phuruangrat, T. Thongtem, S. Thongtem, Analysis of lead molybdate and lead tungstate synthesized by a sonochemical method, Curr. Appl. Phys. 10 (2010) 342–345.

[30] R. Jia, Y. Zhang, Synthesis and optical properties of $PbMoO_4$ nanoplates, Chin. Opt. Lett. 8 (2010) 1152–1155.

[31] W. Jiang, W. Zhu, C. Peng, F. Yang, S. Xuan, X. Gong, Controllable synthesis of hierarchical strontium molybdate by sonochemical method, Cryst. Res. Technol. 47 (2012) 997–1003.

[32] S.M. Hosseinpour-Mashkani, A. Sobhani-Nasab, M. Mehrzad, Controlling the synthesis $SrMoO_4$ nanostructures and investigation its photocatalyst application, J. Mater. Sci. Mater. Electron. 27 (2016) 5758–5763.

[33] V.D. Araújo, R. Tranquilin, F. Motta, C. Paskocimas, M.I.B. Bernardi, L. S. Cavalcante, J. Andres, E. Longo, M. Bomio, Effect of polyvinyl alcohol on the shape, photoluminescence and photocatalytic properties of $PbMoO_4$ microcrystals, Mater. Sci. Semicond. Process. 26 (2014) 425–430.

[34] M. Shkir, Z. Khan, M. Hamdy, H. Algarni, S. AlFaify, A facile microwave-assisted synthesis of $PbMoO_4$ nanoparticles and their key characteristics analysis: a good contender for photocatalytic applications, Mater. Res. Express 5 (2018), 095032.

[35] Y.I. Song, K.T. Lim, G.D. Lee, M.S. Lee, S.S. Hong, Synthesis of $PbMoO_4$ nanoparticles by microwave-assisted hydrothermal process and their photocatalytic activity, J. Nanosci. Nanotechnol. 14 (2014) 8502–8506.

[36] P. Kwolek, K. Pilarczyk, T. Tokarski, M. Łapczyńska, M. Pacia, K. Szaciłowski, Lead molybdate–a promising material for optoelectronics and photocatalysis, J. Mater. Chem. C 3 (2015) 2614–2623.

[37] J. Sczancoski, L. Cavalcante, M. Joya, J.A. Varela, P. Pizani, E. Longo, $SrMoO_4$ powders processed in microwave-hydrothermal: synthesis, characterization and optical properties, Chem. Eng. J. 140 (2008) 632–637.

[38] E. Gomes, L. Gracia, A. Santiago, R. Tranquilin, F. Motta, R. Amoresi, E. Longo, M. Bomio, J. Andres, Structure, electronic properties, morphology evolution, and photocatalytic activity in $PbMoO_4$ and $Pb_{1-2x}Ca_xSr_xMoO_4$ (x= 0.1, 0.2, 0.3, 0.4 and 0.5) solid solutions, Phys. Chem. Chem. Phys. 22 (2020) 25876–25891.

[39] B.H. Toby, EXPGUI, a graphical user interface for GSAS, J. Appl. Crystallogr. 34 (2001) 210–213.

[40] A.M. Huerta-Flores, I. Juárez-Ramírez, L.M. Torres-Martínez, J.E. Carrera-Crespo, T. Gómez-Bustamante, O. Sarabia-Ramos, Synthesis of $AMoO_4$ (A= Ca, Sr, Ba) photocatalysts and their potential application for hydrogen evolution and the degradation of tetracycline in water, J. Photochem. Photobiol. A Chem. 356 (2018) 29–37.

[41] G. Gurgel, L. Lovisa, O. Conceição, M. Li, E. Longo, C. Paskocimas, F. Motta, M. Bomio, Evaluation of morphology and photoluminescent properties of $PbMoO_4$ crystals by ultrasonic amplitude, J. Mater. Sci. 52 (2017) 4608–4620.

[42] M. Buryi, V. Laguta, M. Fasoli, F. Moretti, K. Jurek, M. Trubitsyn, M. Volnianskii, S. Nagorny, V. Shlegel, A. Vedda, Charge trapping processes and energy transfer studied in lead molybdate by EPR and TSL, J. Lumin. 205 (2019) 457–466.

[43] A. Phuruangrat, T. Thongtem, S. Thongtem, Preparation, characterization and photoluminescence of nanocrystalline calcium molybdate, J. Alloy. Compd. 481 (2009) 568–572.

[44] S. Achary, S. Patwe, A. Vishwanath, S. Wajhal, P. Krishna, A.J.M.C. Tyagi, Evolution of crystal structure of $PbMoO_4$ between 5 and 300 K: a low temperature powder neutron diffraction study, Mater. Chem. Phys. 260 (2021), 124111.

[45] Z. Xin, L. Li, X. Zhang, W. Zhang, Microwave-assisted hydrothermal synthesis of chrysanthemum-like Ag/ZnO prismatic nanorods and their photocatalytic properties with multiple modes for dye degradation and hydrogen production, RSC Adv. 8 (2018) 6027–6038.

[46] Z. Li, C. Lu, Z. Xia, Y. Zhou, Z. Luo, X-ray diffraction patterns of graphite and turbostratic carbon, Carbon 45 (2007) 1686–1695. N Y.

[47] J. Revathy, N.C. Priya, K. Sandhya, D.N.J.B.O.M.S. Rajendran, Structural and optical studies of cerium doped gadolinium oxide phosphor, Bull. Mater. Sci. 44 (2021) 1–8.

[48] Y.I. Song, K.T. Lim, G.D. Lee, M.S. Lee, S.S.J.J.O.N. Hong, Synthesis of $PbMoO_4$ nanoparticles by microwave-assisted hydrothermal process and their photocatalytic activity, J. Nanosci. Nanotechnol. 14 (2014) 8502–8506.

[49] T. Siritanon, A. Jiamprasertboon, N. Yong, Structure and optical properties of $Ni_{1-x}Co_xWO_4$ solid solutions, Mater. Lett. 145 (2015) 316–320.

[50] P. Medeiros, A. Santiago, E. Ferreira, M. Li, E. Longo, M. Bomio, F. Motta, Influence Ca-doped $SrIn_2O_4$ powders on photoluminescence property prepared one step by ultrasonic spray pyrolysis, J. Alloy. Compd. 747 (2018) 1078–1087.

[51] G. Gaidamavičienė, A. Žalga, Synthesis, a structural and thermoanalytical study of $Ca_{1-x}Sr_xMoO_4$ ceramic, Mater. Chem. Phys. 241 (2020), 122339.

[52] K. Momma, F. Izumi, VESTA 3 for three-dimensional visualization of crystal, volumetric and morphology data, J. Appl. Crystallogr. 44 (2011) 1272–1276.

[53] M. Rada, S. Rada, P. Pascuta, E. Culea, Structural properties of molybdenum-lead-borate glasses, Spectrochim. Acta A Mol. Biomol. Spectrosc. 77 (2010) 832–837.

[54] L.K. Bharat, G.S.R. Raju, J.S. Yu, Red and green colors emitting spherical-shaped calcium molybdate nanophosphors for enhanced latent fingerprint detection, Sci. Rep. 7 (2017) 1–14.

[55] S.K. Gupta, M. Sahu, P. Ghosh, D. Tyagi, M. Saxena, R. Kadam, Energy transfer dynamics and luminescence properties of Eu^{3+} in $CaMoO_4$ and $SrMoO_4$, J. Chem. Soc. Dalton Trans. 44 (2015) 18957–18969.

[56] T. Thongtem, S. Kungwankunakorn, B. Kuntalue, A. Phuruangrat, S. Thongtem, Luminescence and absorbance of highly crystalline $CaMoO_4$, $SrMoO_4$, $CaWO_4$ and $SrWO_4$ nanoparticles synthesized by co-precipitation method at room temperature, J. Alloy. Compd. 506 (2010) 475–481.

[57] J. Sczancoski, M. Bomio, L. Cavalcante, M. Joya, P. Pizani, J.A. Varela, E. Longo, M.S. Li, J. Andrés, Morphology and blue photoluminescence emission of $PbMoO_4$ processed in conventional hydrothermal, J. Phys. Chem. C 113 (2009) 5812–5822.

[58] S. Ayni, M. Sabet, M. Salavati-Niasari, Synthesis and characterization of lead molybdate nanostructures with high photocatalytic activity via simple co-precipitation method, J. Clust. Sci. 27 (2016) 315–326.

[59] M. Shen, Q. Zhang, H. Chen, T. Peng, Hydrothermal fabrication of $PbMoO_4$ microcrystals with exposed (001) facets and its enhanced photocatalytic properties, CrystEngComm 13 (2011) 2785–2791.

[60] Z. Yang, C. Hou, G. Duan, F. Yang, P. Liu, C. Wang, L. Liu, G. Dong, The photoluminescent property and optical transition analysis of host sensitized $Ca_{0.5}Sr_{0.5}MoO_4$:dy^{3+} phosphor, J. Alloy. Compd. 604 (2014) 346–351.

[61] M. Rahimi-Nasrabadi, Strontium molybdate nanostructures: synthesis of different shapes through a new approach and its photocatalyst application, J. Mater. Sci. Mater. Electron. 28 (2017) 2200–2205.

[62] D. Wood, J. Tauc, Weak absorption tails in amorphous semiconductors, Phys. Rev. B 5 (1972) 3144.

[63] M. Bomio, L.S. Cavalcante, M. Almeida, R. Tranquilin, N. Batista, P.S. Pizani, M. S. Li, J. Andres, E. Longo, Structural refinement, growth mechanism, infrared/ Raman spectroscopies and photoluminescence properties of $PbMoO_4$ crystals, Polyhedron 50 (2013) 532–545.

[64] R.S. Datta, J.Z. Ou, M. Mohiuddin, B.J. Carey, B.Y. Zhang, H. Khan, N. Syed, A. Zavabeti, F. Haque, T. Daeneke, Two dimensional $PbMoO_4$: a photocatalytic material derived from a naturally non-layered crystal, Nano Energy 49 (2018) 237–246.

[65] F. Nobre, R. Muniz, F. Martins, B. Silva, J. de Matos, E. da Silva, P. Couceiro, W. Brito, Y. Leyet, Calcium molybdate: toxicity and genotoxicity assay in Drosophila melanogaster by SMART test, J. Mol. Struct. 1200 (2020), 127096.

[66] R. Künzel, N.K. Umisedo, E. Okuno, E.M. Yoshimura, A.P. de Azevedo Marques, Effects of microwave-assisted hydrothermal treatment and beta particles irradiation on the thermoluminescence and optically stimulated luminescence of $SrMoO_4$ powders, Ceram. Int. (2020).

[67] D.F. Dos Santos, L.X. Lovisa, A.D.A.G. Santiago, M.S. Li, E. Longo, M. Bomio, F.V. D. Motta, Growth mechanism and vibrational and optical properties of $SrMoO_4$: tb^{3+}, Sm^{3+} particles: green–orange tunable color, J. Mater. Chem. 55 (2020) 8610–8629.

[68] P. Yu, G.B. Hu, Y.F. Tian, D.Q. Xiao, Y. Liu, Q.W. Guo, Synthesis and photoluminescent properties of nanocrystalline $CaMoO_4$ thin film via chemical solution processing, J. Nanosci. Nanotechnol. 8 (2008) 2651–2654.

[69] G. Blasse, B.C. Grabmaier, A General Introduction to. Luminescent Materials, Luminescent Materials, Springer, Berlin, Heidelberg, 1994.